PAPER

Check for updates

Uranyl (UO$_2^{2+}$) structuring and dynamics at graphene/electrolyte interface†

Nitesh Kumar [iD]

The physicochemical phenomena at the solid/electrolyte interfaces govern various industrial processes ranging from energy generation, storage, and catalysis to chemical separations and purification. Adsorption-based solid/liquid extraction methods are promising for the selective and rapid separation of nuclear (such as uranium) and other critical materials. In this study, we quantified the adsorption, complexation, and dynamics of UO$_2^{2+}$ ions on the graphene surface in various electrolyte media (LiNO$_3$, NaNO$_3$ and CsNO$_3$) using all-atom molecular dynamics simulations, in combination with network theory based subensemble analysis, enhanced sampling, and temporal analysis. We observe that the choice of background electrolyte impacts the propensity of UO$_2^{2+}$ adsorption on the graphene surface, with LiNO$_3$ being the most favorable at both low and high uranyl–nitrate concentrations. Even though UO$_2^{2+}$ primarily retained its coordination with water and interacted via the outer-sphere mechanism with graphene, the interfacial segregation of NO$_3^-$ increased the number of contact ion pairs (CIPs) between UO$_2^{2+}$ and NO$_3^-$ ions, and the residence times of UO$_2^{2+}$ within the interfacial region. This study provides a fundamental understanding of the structure and dynamics of UO$_2^{2+}$ on the solid surface necessary to design advanced adsorption-based separation methods for energy-relevant materials.

1 Introduction

U^{6+} generally present as uranyl (UO$_2^{2+}$) ions in aqueous media is one of the most common radionuclides present in nuclear waste and seawater.[1–3] Multiple separation techniques, such as liquid/liquid extraction, ion exchange, membrane processing, supramolecular extraction, *etc.*, have been used for the selective extraction of the UO$_2^{2+}$ ions.[4–8] With advances in adsorption-based separation methods, graphene, and its functionalized forms are now considered promising adsorbents for the separation of UO$_2^{2+}$ even at low concentrations.[9–14] However, a detailed understanding of the chemistry associated with UO$_2^{2+}$ adsorption, complexation, and dynamics at the graphene/electrolyte surface is lacking. Recent developments reveal ion adsorption at biphasic interfaces to be independent of the Hofmeister trend.[15,16] As such, Cole *et al.*[17] showed segregation of both H$_3$O$^+$ and OH$^-$ ions at the graphene/aqueous interface following surfactant-like behavior. Jungwirth and Tobias *et al.* showed the favorability of large polarizable halide ions such as I$^-$ and Br$^-$ (with loose water coordination) over smaller ones (Cl$^-$ and F$^-$) for adsorption at liquid/liquid interfaces.[18–20] A recent study of UO$_2^{2+}$ at the hexane/LiNO$_{3(aq)}$

interface revealed an increased uranyl complexation with nitrate to form mono- or di-nitrate uranyl⋯nitrate complexes. The residence times of UO$_2^{2+}$ within the interfacial region were longer compared to the bulk aqueous phase, and further increased with higher LiNO$_3$ concentrations. This suggests that NO$_3^-$ ions cooperatively influence the interfacial behavior of UO$_2^{2+}$ ions.[21] However, the effects of counterion cooperativity on adsorption at solid/liquid interfaces like graphene/electrolyte are not well understood, including how favorable NO$_3^-$ adsorption[22,23] and ion gradients influence UO$_2^{2+}$ co-adsorption, complexation and dynamic at the pure graphene/electrolyte interfaces.[24]

Polarization of ions, especially at the graphene surface, affects the adsorption and dynamics in the interfacial region. Accurate modeling of the adsorption behavior of actinide ions requires the inclusion of polarization effects either explicitly or implicitly within the force fields.[25] One of the methods is to construct system-specific polarizable force fields for ions, water, and graphene. However, the parameterization of the polarizable force fields for concentrated electrolyte systems is computationally expensive and time-consuming. Various methods have been used to indirectly account for polarization effects, such as including polarizability only to ions,[17,26] or optimizing ion–graphene (ion–π) interactions by tuning the Lennard-Jones ($\varepsilon_{i\text{-}c}$) parameter based on the DFT free energies of adsorption and charge transfer.[27] Recent studies have accounted for the electronic polarization effects using electronic continuum correction (ECC) methodology that involves

Department of Chemistry, Washington State University, Pullman, Washington 99163, USA. E-mail: nitesh.kumar@wsu.edu, kmnitesh05@gmail.com

† Electronic supplementary information (ESI) available: System configuration; force fields benchmarking; normalized density profiles, average residence times, density profiles of lithium complexes. See DOI: https://doi.org/10.1039/d4cp02108h

scaling of the ion charges (q_i) in the nonbonded potential terms of the nonpolarizable models.[28] The ECC methodology is extensively benchmarked with experiments and has improved bulk and interfacial properties compared to traditional nonpolarizable force fields.[28] Therefore, we utilized ECC UO_2^{2+} /nitrate force fields, optimized to reproduce the experimental first and second uranyl–nitrate association constants, K_1 and K_2, in 1–5 M $LiNO_3$ solutions.[20,28] Moreover, the amber force fields in combination with the TIP3P water model showed a similar distribution of water at the graphene surface as observed using *ab initio* molecular dynamics simulations.[29]

Extensive efforts have been dedicated to understanding the behavior of ions and other molecules at solid/liquid interfaces through experimental techniques such as vibrational sum frequency generation (VSFG) or X-ray scattering, alongside atomistic simulations.[30–37] However, these characterizations often focus on ensemble-averaged properties. The radioactive nature of uranium further complicates experimental design. Thus, molecular dynamics simulations are crucial for providing detailed microscopic insights into ion behavior at interfaces, guiding experimental setup, and analyses. Using subensemble analysis with network theory, enhanced sampling, and temporal analysis, we characterize the microscopic behavior of uranyl ions at the graphene surface, providing details typically inaccessible with current experimental techniques. Herein, we employed all-atom molecular dynamics simulations to investigate the impact of different nitrate-based electrolyte media on adsorption, complexation, and dynamics of UO_2^{2+} at the graphene/electrolyte interface. To the best of our knowledge, this study represents the first detailed characterization of uranyl behavior at a pure graphene/electrolyte interface. Here, we compared UO_2^{2+} adsorption in various electrolyte mediums, such as $LiNO_3$, $NaNO_3$, and $CsNO_3$, and with low and high uranyl–nitrate concentrations to understand the impact of background electrolyte on the adsorption behavior of UO_2^{2+} at the graphene surface. We utilized NO_3^- in combinations with alkali metal ions, owing to the frequent use of uranyl salts in nitrate media. UO_2^{2+} is observed to adsorb favorably in the interfacial region of the graphene/electrolyte surface. Its density is affected by the choice of background electrolyte, influencing its residence times at the interface. Hydration-mediated ion–graphene interactions in combination with NO_3^- cooperativity, as a result of anionic excess, collectively impact UO_2^{2+} adsorption propensity and complexation in the interfacial region.

2 Results and discussion

2.1 Cooperative adsorption, orientation, and dynamics

The UO_2^{2+} adsorption behavior at the graphene/electrolyte interface at both low (0.36 M) and high (1.08 M) uranyl–nitrate concentration is characterized using the normalized density profiles along the z axis as

$$\rho_\alpha(z) = \frac{\sum\limits_{i \in \alpha} \delta(z_i - z)}{\rho_b}, \qquad (1)$$
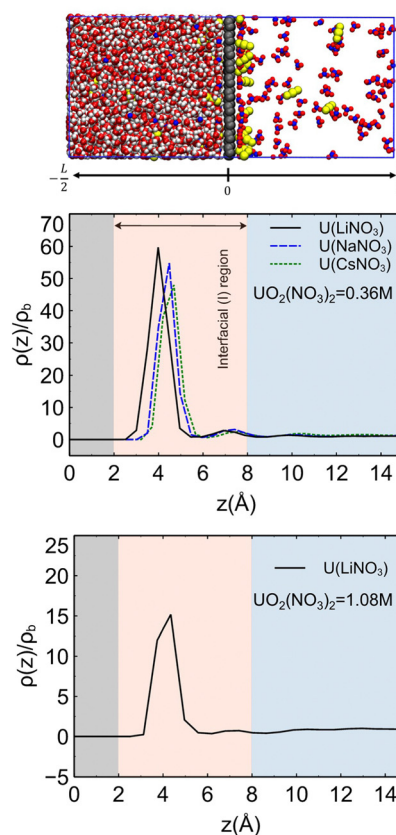

Fig. 1 Simulation snapshot illustrating the adsorption of UO_2^{2+} (yellow) at the graphene/electrolyte interface (upper panel). Oxygen (O), nitrogen (N), and carbon (C) atoms are shown in red, blue, and grey colors respectively. H_2O between 0 and L/2 are hidden for visual clarity. The normalized density profiles (ρ_z) of UO_2^{2+} along the z axis in various 1.41 M electrolytic systems ($LiNO_3$, $NaNO_3$ and $CsNO_3$) and 0.36 M $UO_2(NO_3)_2$ (middle panel) and 1.08 M $UO_2(NO_3)_2$ (lower panel). The densities are normalized by the bulk UO_2^{2+} density, ρ_b. Graphene, interfacial (I), and bulk regions are shown in grey, pink, and blue respectively.

where δ is the Dirac delta function, the sum is applied to all atoms i. ρ_b is the number density in the bulk aqueous phase. The z-position of the graphene sheet is used as a reference point (z_0). At the low uranyl–nitrate concentration of 0.36 M, we observe a UO_2^{2+} excess with a density of almost 45 to 60× in the interfacial region (ranging from 2 to 8 Å) relative to the bulk, depending on the choice of background electrolyte. The highest density of interfacial UO_2^{2+} is obtained in the system with $LiNO_3$, favoring UO_2^{2+} adsorption to the extent of 60× more relative to the bulk. Interestingly, the adsorption propensity of UO_2^{2+} was inversely correlated with the radii of the cation of the background electrolyte as ($LiNO_3$ > $NaNO_3$ > $CsNO_3$), with a respective increase of almost 60, 55, & 45 times relative to the bulk (Fig. 1). At higher uranyl–nitrate concentration of 1.08 M, the UO_2^{2+} density in the interfacial region is ∼15× higher than in the bulk.

Interestingly, we observe a shift in the location of UO_2^{2+} density maxima for different electrolytes. The maximum of the UO_2^{2+} density in the $LiNO_3$ system is found closer to the graphene surface than in the $CsNO_3$ system (Fig. 1). This shift is

associated with the ability of Cs^+ ions to lose their coordinated water, resulting in a higher density of Cs^+ near the graphene surface compared to Li^+ ions. Consequently, this increases competition for UO_2^{2+} ions to adsorb near the graphene surface. We infer that the enhanced density of UO_2^{2+} on the graphene surface is a collective result of the interactions of UO_2^{2+} with the graphene surface as a result of outer-sphere ion–π interactions mediated by the interfacial water and the cooperativity by the adsorbed NO_3^- ions.

To understand the ion enrichment in the interfacial region **I**, we calculated the surface excess Γ_i as

$$\Gamma_i = \int_{z_0}^{z'} \mathrm{d}z \left(\frac{\rho_i(z)}{\rho_i^b} - 1 \right)$$

where $\rho_i(z)$ and ρ_i^b are the density of ions along the z axis and in the bulk, respectively. z_0 is the z position of the graphene sheet, z' is the upper limit of the region S_2, *i.e.*, $z_{S_2} = 8$ Å. The values of Γ_i are directly correlated with the enhancement of the ions in the interfacial region (S_1 and S_2 as shown in Fig. 2). In each system, NO_3^- showed a substantial enhancement compared to alkali metal ions M^+ (Fig. 2). Interestingly, the surface excess of UO_2^{2+} followed the same trend as NO_3^-, that is, ($LiNO_3 >$, $NaNO_3 >$, $CsNO_3$), showing cooperativity in adsorption behavior. The excess of NO_3^- attracted UO_2^{2+}, causing an increase in the concentration gradient of UO_2^{2+} at the interface. The Γ_i of the interfacial M^+ followed the ion charge density trend *i.e.*, $Cs^+ > Na^+ > Li^+$. The Γ_i (M^+) trend correlates with the ability of cations to lose water coordination in the interfacial region. The extent of cooperative NO_3^- effects on UO_2^{2+} will decrease due to competition by Cs^+ ions for surface adsorption.[38] As such, the relatively higher density and competition from the Cs^+ ions at the interface created a screening layer and made it difficult for NO_3^- and UO_2^{2+} to adsorb directly on the graphene surface, as illustrated by a lower density of NO_3^- or UO_2^{2+} in the system with Cs^+ relative to Li^+ (Fig. 2 Right panel).

Next, we present the orientation distribution of the $\overrightarrow{UO}$ vector along a unit vector perpendicular to the graphene surface (as shown in the inset of Fig. 3) in the interfacial and bulk regions. Angles $0°$ and $90°$ represent the respective perpendicular and parallel orientations relative to the graphene surface. A high probability of $\cos \geq 0.5$ or ≤ -0.5 shows a favorability
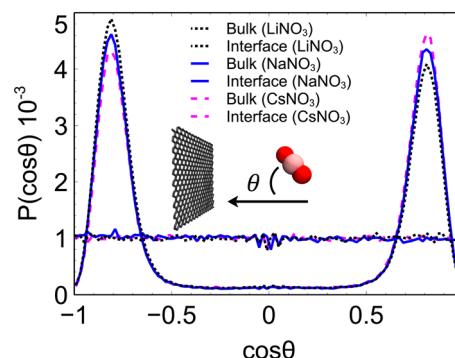

Fig. 3 The comparison of the UO_2^{2+} orientation probability distributions in bulk and at the electrolyte/graphene interfacial region **I**, with different electrolyte media. The error bars were computed using block averaging methodology. The definition of θ is provided in the inset.

of the orientation of UO_2^{2+} perpendicular to the graphene sheet. Therefore, the highest probability of orientation at ~ 0.7 shows its preferable orientation at $\sim 45°$. Greathouse *et al.* reported a UO_2^{2+} orientation of $\sim 45°$ at the surface of quartz (101).[39] Interestingly, the choice of background electrolyte has only a minor effect on the orientation of interfacial UO_2^{2+}.

To characterize the role of the increased density of interfacial UO_2^{2+} on its interfacial dynamics, we quantified the UO_2^{2+} residence in the interfacial regions by calculating the average time spent in the given slab of size 2 Å.[21] The survival probability is given by

$$P(t) = \frac{N(t, \Delta t)}{\sum_t N(t, \Delta t)} \qquad (2)$$

$N(t,\Delta t)$ is the continuous-time duration of the ions in the respective slabs. The average residence time τ is computed as

$$\tau = \int_0^\infty t P(t) \mathrm{d}t, \qquad (3)$$

UO_2^{2+} residence time, τ (UO_2^{2+}), in various interfacial slabs is shown in Table S1 (ESI†). On average, UO_2^{2+} spent ~ 590 ps at the graphene/electrolyte interface compared to 86.64 ps on an analogous hexane surface with a similar system composition using $LiNO_3$ as the background electrolyte.[21] A $\sim 7\times$ increase in
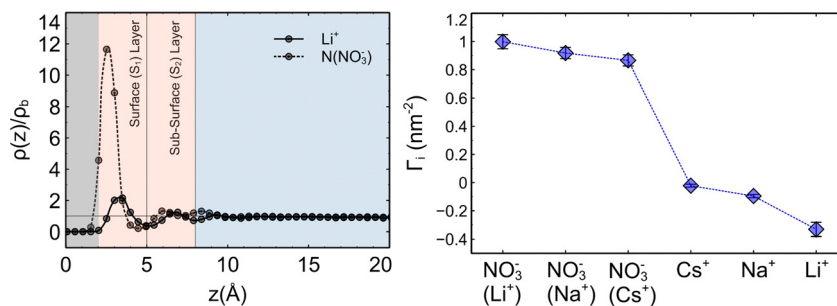

Fig. 2 The normalized density profiles of Li^+ and NO_3^- (ρ_z) along the z axis (left panel). The surface excess Γ_i of ions at the graphene/electrolyte interface (right panel). The interfacial region **I**, ranging from 2 to 8 Å is divided into two sublayers, S_1 (2−5 Å) and S_2 (5−8 Å), based on layering formed by the background electrolyte as shown in the left panel.

τ at the graphene compared to the hexane interface clearly shows the favorability of UO_2^{2+} for the graphene surface adsorption primarily due to favorable adsorption of uranyl at graphene/electrolyte interface.[21]

2.2 Ion complexation at the graphene surface

To understand how the ion concentration gradient alters UO_2^{2+} complexation with NO_3^- at the graphene/electrolyte interface, the time-averaged number densities of individual $[UO_2(NO_3)_n]^{(2-n)+}$ ion pairs along the z axis are plotted in Fig. 4. The computation of these profiles involved three major steps: (1) the creation of UO_2^{2+}–NO_3^- connectivity networks, using r(U-NO) = 3.91 Å cutoff; (2) the characterization of $[UO_2(NO_3)_n]^{(2-n)+}$ complexes using the graph theory[40,41]; (3) the binning of complex densities along the z-axis (bin size 0.2 Å, normalized by the volume of the bin) using the atomic coordinates of the U atoms involved in the $[UO_2(NO_3)_n]^{(2-n)+}$ complexes. The methodology is described in detail in ref. 42. Experimental and computational studies revealed that UO_2^{2+} interact strongly with five H_2O in the bulk aqueous phase under infinite dilution conditions.[43,44] Within the electrolyte or acidic media, UO_2^{2+} complex weakly with NO_3^- to form $[UO_2(NO_3)]^+$ and $[UO_2(NO_3)_2]$ complexes with their respective association constants K_1 and K_2 in range 0.1–0.6 and 0.02–0.04 respectively.[21,45–47] Interestingly, UO_2^{2+} preserves its water coordination at the graphene surface, (Fig. 4), resulting in outer-sphere interactions with the graphene surface. In the bulk and interfacial region, the five coordinated $[UO_2(NO_3)_0(H_2O)_5]^{2+}$ remained the most probable, followed by the mono-nitrate complexes. A similar trend is observed for the uranyl···nitrate complexation at the hexane/electrolyte interface.[21]

Importantly, the propensity of UO_2^{2+} complexes with NO_3^- is higher for the graphene surface compared to the bulk, as revealed by the higher densities of both $[UO_2(NO_3)_1]^+$ and $[UO_2(NO_3)_2]$ complexes in the interfacial region (Fig. 4). This increase is associated with the greater availability of nitrate ions for complexation, change in electrolyte concentration, and water structuring (*vide-infra*) near to the interface.

The impact of concentration gradients on the ion-pairing of the adsorbed Li^+ is studied in terms of Li^+···NO_3^- number density profiles along the z axis, using the graph theory

approach analogous to the one used for UO_2^{2+}. The coordination of Li^+ with NO_3^- is described using the distance of the first minima in the respective pair correlation functions, *i.e.* r_{cut} of 3.5 Å for $N(NO_3^-)$. Fig. S2 (ESI†) shows the time-averaged number densities profiles of $[Li(NO_3)_n]^{(1-n)+}$ ($n = 0-1$) complexes along the z axis. The results in Fig. S2 (ESI†) show that unlike UO_2^{2+}, the interfacial concentration gradient significantly alters the Li^+ solvation shell, causing an increase in the density of $LiNO_3$ CIPs near the graphene surface. It is revealed that the Li^+ present in the region S_1 showed enhanced density of CIPs compared to the region S_2 or the bulk aqueous phase. The enhanced ion···ion interactions of Li^+···NO_3^- is related to NO_3^- excess within the S_1 surface region.

2.3 Water structure and topology

The average local structure of water at the dynamically evolving graphene/electrolyte interface is characterized using the orientation and the hydrogen bond (HB) network of water in the interfacial region.[48,49] The dipole orientation of water along the z axis is calculated using

$$\langle \cos(\theta_i) \rangle = \left\langle \sum_i \hat{\mu}_i \cdot \hat{n}_z \right\rangle$$

where, $\cos(\theta_i)$ is the angle between the unit H_2O dipole vector i, $\hat{\mu}_i$ and a unit vector normal to the xy plane. The orientation of water in various electrolyte media is plotted in Fig. 5. The water has an anisotropic orientation pattern in the surface region S_1 that extends to the subsurface region S_2. The average values of $\cos\theta \sim 0.2$ show a preferential parallel orientation of the water dipole vector along the surface normal vector, which is consistent with the cos values reported in the literature.[49,50] The interfacial water molecules are oriented in such a way that the H atoms face the graphene surface and the O atoms face the bulk aqueous phase. The orientation of H_2O remained almost unaffected by the choice of electrolyte. Enhanced ion density in the interfacial region can alter the water HB network. The structure of water in the interfacial region has been studied in terms of changes in average HB with the change in the distance from the surface in $LiNO_3$ electrolyte media.[51] Layered distributions of average HB were reported for the water network as a result of dangling water molecules, which were correlated with the distribution of water density in the interfacial region.[50–52] Here, we report densities of various $(H_2O)_n$ HBs along the z axis. H-bonding of water in the surface (S_1) subsurface (S_2) region and bulk is compared using the average number density of water forming 0–4 HBs along the z axis. H-bonding network of H_2O is computed using a combined distance and angle-based geometric criterion. HBs were defined based on O···H distance cutoff of 2.5 Å and an O···H–O angle in range 145–180°. The strong structure of water molecules in the vicinity of the graphene layer leads to dramatic variations in the HB pattern that range up to three interfacial layers of 3 Å. The highest population of water molecules in the S_1 & S_2 region formed 2 HBs compared to the bulk, where the highest number of water formed 3 HBs in the bulk aqueous
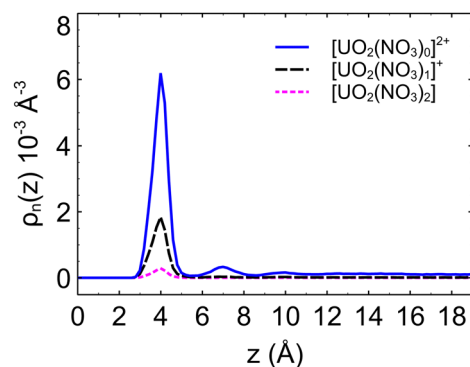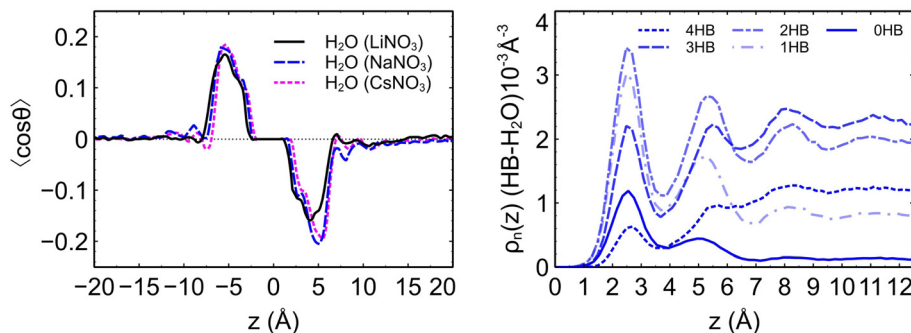

Fig. 4 Average number density of $[UO_2(NO_3)_n]^{(2-n)+}$ ($n = 0, 2$) complexes along the z axis in the system with $LiNO_3$.

Fig. 5 (left panel) Average dipole orientation profiles of H_2O along the z axis in various electrolyte media in the presence of UO_2^{2+} ions. (right panel) Average number densities of the H_2O in different H-bonding states along z axis in the electrolytic system with $LiNO_3$.

phase. More specifically, the water molecules present in the S_1 region formed HBs in order 2 > 1 > 3 > 0 > 4. Interestingly, the region S_1 contained a significant population of water molecules that did not form HB. The breakdown of the H-bonding network in S_1 and S_2 is directly linked to the stratified water structure in the interfacial region, which in turn is associated with the layered ion adsorption behavior observed at the graphene/electrolyte interface.

2.4 Favorable interactions with graphene

The adsorption affinity of UO_2^{2+} and Li^+ towards graphene is studied using the potential of mean force simulations under infinite dilution conditions using one ion-pair (Fig. 6). The z-distance between ion and graphene is used as the collective variable, as detailed in the ESI.† The presence of minima in the region 4–5 Å shows that the adsorption of UO_2^{2+} is favored by outer-sphere (interfacial water-mediated) ion–graphene inter-actions. A wide and stable region is observed with a depth of -0.812 kcal mol^{-1} for the UO_2^{2+} adsorption at the graphene surface. In comparison, the free energy for the Li^+ adsorption is observed to be -0.496 kcal mol^{-1}, the PMF of which exhibits a broad minimum, shifted to a smaller distance from the gra-phene surface (Fig. 6). The UO_2^{2+} interactions with graphene are more significant and longer than Li^+, persisting up to 10 Å from the surface of the graphene, as a result of stronger cation–π

interactions accounted within the non-bonded parameters.[15] The increased density of UO_2^{2+} in the **I** region correlates with the favorable free energy of adsorption. Therefore, the preferential adsorption of UO_2^{2+} at graphene is a collective influence of thermodynamic stability and cooperation by the background electrolyte towards the UO_2^{2+} adsorption at graphene.

3 Conclusions

Molecular dynamics simulations were performed with ECC-optimized force fields to analyze the adsorption, complexation, and dynamics of UO_2^{2+} ions at graphene/electrolyte interface under different electrolyte media ($LiNO_3$, $NaNO_3$, and $CsNO_3$). Our findings highlight that ion–graphene interactions, coupled with the type of background electrolyte, including favorable NO_3^- graphene adsorption influence UO_2^{2+} surface excess. Notably, $LiNO_3$ demonstrated the greatest efficacy in promoting UO_2^{2+} adsorption. The potential of mean force simulations reveal that UO_2^{2+} exhibit enhanced stability at the graphene interface relative to Li^+. The cooperativity of NO_3^- plays an important role in this process by increasing the residence times of uranyl, and the total number of CIPs between uranyl and nitrate in the interfacial region. In future work, exploring the role of electrolyte concen-tration and the choice of anions will provide a deeper under-standing of how anions influence uranyl adsorption and dynamics near the graphene surface. The fundamental microscopic-level insights of uranyl adsorption, speciation, and dynamics presented in this study are crucial for developing effective adsorption-based techniques for selective uranyl separation from seawater or nuclear waste and guiding future separations research.

4 Materials and methods

All-atom molecular dynamics simulations were performed using the GROMACS-2018.2 software package.[53] Initial systems composed of 5022 TIP3P H_2O, 130 M^+ ($M^+ = Li^+$, Na^+ & Cs^+) ions (1.41 M), 32 UO_2^{2+}, 194 NO_3^- ions (0.36 M) and a graphene sheet were generated using the Packmol software package.[54] The ions and water molecules were randomly placed in an aqueous phase with dimensions $36.8 \times 42.3 \times 98.1$ Å^3. Periodic bound-ary conditions were implemented in all three directions. Each
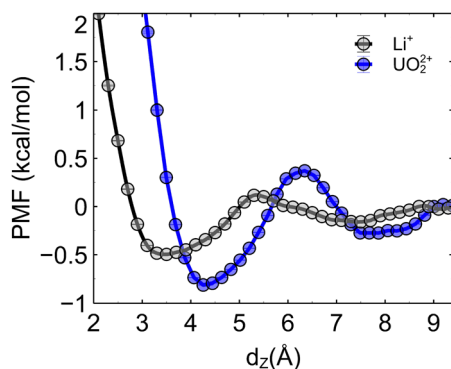

Fig. 6 Potential of mean forces (PMFs) of Li^+ and UO_2^{2+} along the z-distance perpendicular to graphene (d_z). The collective variable d_z is described in the ESI.†

system was equilibrated in NPT and NVT for 20 ns, followed by 40 ns production runs. Molecular dynamics were performed at 298 K using a leap-frog integrator with a 2 fs time step. The temperature selection aimed to replicate the conditions for uranyl extraction from seawater. However, other experimental conditions may require elevated temperatures. At elevated temperatures, variations in interfacial water structure and ion adsorption are anticipated, potentially increasing adsorption/desorption kinetics or weakening uranyl–nitrate complexation due to thermal fluctuations. Although the polarizability of water and graphene has a negligible effect on the structure and dynamics of water at the interface,[51] the presence of an electrolyte can create ion solvent polarization and graphene polarization. The polarizable force fields for heavy-metal ions and graphene are more computationally demanding than non-polarizable. To overcome cost barriers, Williams *et al.*[27] recently treated polarization effects by scaling Lennard-Jones parameters between graphene and ions. Alternatively, system polarization can be treated explicitly using electronic continuum correction (ECC) methodology by scaling ion charges q_i.[28] In this study, the simulations were performed using the parameters extensively benchmarked to reproduce the experimental uranyl–nitrate first and second association constants (K_1 and K_2) using the ECC methodology.[21] This methodology is performed on Joung *et al.* force fields for alkali metal ions[55] *i.e.* Li$^+$, Na$^+$ & Cs$^+$ by scaling the charges to 90% of their original values to account for the polarization effects. Water is modeled using the TIP3P model in each simulated system.[56] The graphene layer was modeled and compared using the AMBER99[57] and CHARMM36[58] force fields. Both force fields exhibited similar behavior, and a detailed comparison is provided in the ESI.† Amber99 force field for graphene is used in the final production runs. Non-bonded interactions were truncated to r = 1.6 nm. The particle mesh Ewald (PME) summation methodology is used for long-range electrostatic interactions.

4.1 Impact of ion charges on surface adsorption

To probe the sensitivity of the UO$_2^{2+}$ adsorption towards the ion charges q_i, the charges on UO$_2^{2+}$, Li$^+$ and NO$_3^-$ were scaled from 80% to 95% (with an increment of 5%) of the initial Joung-Wipff combination of force fields.[55,59,60] We plotted the density of UO$_2^{2+}$ at the graphene surface varied with q_i. We observe a dependence of ion charge on the adsorption behavior of UO$_2^{2+}$ at the interface, which is directly related to an enhancement in ion association within the interfacial region, similar to what was previously observed at the hexane/electrolyte interface.[21] For each q_i, the normalized density profiles reveal a UO$_2^{2+}$ excess in the interfacial region, with a UO$_2^{2+}$ density around 30 times greater than the bulk with no charge scaling, and around 15 times greater density at 80% charge scaling (Fig. S1, ESI†). Recently, we demonstrated that a charge scaling factor of 0.9 (applied to Joung-Wipff *et al.* force fields) reproduced experimental UO$_2^{2+}$–NO$_3^-$ association constants (in LiNO$_3$). To keep the consistency, we employed the same charge scaling of 0.9 to the ion force fields in this study.[21]

Data availability

All data generated in this study, as well as details regarding the algorithms and software used, are included either within the main text of the paper or in the ESI.†

Conflicts of interest

There are no conflicts to declare.

Acknowledgements

References

1 Y. Lu, Coordination chemistry in the ocean, *Nat. Chem.*, 2014, **6**, 175–177.

2 R. C. Ewing, W. J. Weber and F. W. Clinard Jr, Radiation effects in nuclear waste forms for high-level radioactive waste, *Prog. Nucl. Energy*, 1995, **29**, 63–127.

3 T. P. Rao, P. Metilda and J. M. Gladis, Preconcentration techniques for uranium (VI) and thorium (IV) prior to analytical determination—an overview, *Talanta*, 2006, **68**, 1047–1064.

4 B. Gu, Y.-K. Ku and P. M. Jardine, Sorption and binary exchange of nitrate, sulfate, and uranium on an anion-exchange resin, *Environ. Sci. Technol.*, 2004, **38**, 3184–3188.

5 J. Wang and S. Zhuang, Extraction and adsorption of U (VI) from aqueous solution using affinity ligand-based technologies: an overview, *Rev. Environ. Sci. Bio/Technol.*, 2019, **18**, 437–452.

6 C. Tsouris, Uranium extraction: fuel from seawater, *Nat. Energy*, 2017, **2**, 1–3.

7 A. Uysal, Aqueous interfaces in chemical separations, *Langmuir*, 2023, **39**, 17570–17580.

8 D. S. Sisodiya, S. M. Ali and A. Chattopadhyay, Unexplored Isomerization Pathways of Azobis (benzo-15- crown-5): Computational Studies on a Butterfly Crown Ether. The, *J. Phys. Chem. A*, 2023, **127**, 7080–7093.

9 G. Zhao, T. Wen, X. Yang, S. Yang, J. Liao, J. Hu, D. Shao and X. Wang, Preconcentration of U (VI) ions on few-layered graphene oxide nanosheets from aqueous solutions, *Dalton Trans.*, 2012, **41**, 6182–6188.

10 Q.-Y. Wu, J.-H. Lan, C.-Z. Wang, C.-L. Xiao, Y.-L. Zhao, Y.-Z. Wei, Z.-F. Chai and W.-Q. Shi, Understanding the bonding nature of uranyl ion and functionalized graphene: a theoretical study, *J. Phys. Chem. A*, 2014, **118**, 2149–2158.

11 P. Zong, S. Wang, Y. Zhao, H. Wang, H. Pan and C. He, Synthesis and application of magnetic graphene/iron oxides

composite for the removal of U (VI) from aqueous solutions, *Chem. Eng. J.*, 2013, **220**, 45–52.

12 A. Deb, P. Ilaiyaraja, D. Ponraju and B. Venkatraman, Diglycolamide functionalized multi-walled carbon nanotubes for removal of uranium from aqueous solution by adsorption, *J. Radioanal. Nucl. Chem.*, 2012, **291**, 877–883.

13 I. I. Fasfous and J. N. Dawoud, Uranium (VI) sorption by multiwalled carbon nanotubes from aqueous solution, *Appl. Surf. Sci.*, 2012, **259**, 433–440.

14 T. Maity, A. Aggarwal, S. Dasgupta, V. Velachi, A. K. Singha Deb, S. M. Ali and P. K. Maiti, Efficient Removal of Uranyl Ions Using PAMAM Dendrimer: Simulation and Experiment, *Langmuir*, 2023, **39**, 6794–6802.

15 D. L. McCaffrey, S. C. Nguyen, S. J. Cox, H. Weller, A. P. Alivisatos, P. L. Geissler and R. J. Saykally, Mechanism of ion adsorption to aqueous interfaces: Graphene/water vs. air/water, *Proc. Natl. Acad. Sci. U. S. A.*, 2017, **114**, 13369–13373.

16 N. Schwierz, D. Horinek and R. R. Netz, Reversed anionic Hofmeister series: the interplay of surface charge and surface polarity, *Langmuir*, 2010, **26**, 7370–7379.

17 D. J. Cole, P. K. Ang and K. P. Loh, Ion adsorption at the graphene/electrolyte interface, *J. Phys. Chem. Lett.*, 2011, **2**, 1799–1803.

18 P. Jungwirth and D. J. Tobias, Specific ion effects at the air/water interface, *Chem. Rev.*, 2006, **106**, 1259–1281.

19 P. Jungwirth and D. J. Tobias, Ions at the air/water interface, *J. Phys. Chem. B*, 2002, **106**, 6361–6373.

20 M. Vazdar, E. Pluharova, P. E. Mason, R. Vácha and P. Jungwirth, Ions at hydrophobic aqueous interfaces: Molecular dynamics with effective polarization, *J. Phys. Chem. Lett.*, 2012, **3**, 2087–2091.

21 N. Kumar, M. J. Servis and A. E. Clark, Uranyl Speciation in the Presence of Specific Ion Gradients at the Electrolyte/Organic Interface, *Solvent Extr. Ion Exch.*, 2022, **40**, 165–187.

22 W. Hua, D. Verreault and H. C. Allen, Surface electric fields of aqueous solutions of NH_4NO_3, $Mg (NO_3)_2$, $NaNO_3$, and $LiNO_3$: implications for atmospheric aerosol chemistry, *J. Phys. Chem. C*, 2014, **118**, 24941–24949.

23 P. Ganesan, R. Kamaraj and S. Vasudevan, Application of isotherm, kinetic and thermodynamic models for the adsorption of nitrate ions on graphene from aqueous solution, *J. Taiwan Inst. Chem. Eng.*, 2013, **44**, 808–814.

24 N. Kumar, M. J. Servis, Z. Liu and A. E. Clark, Competitive interactions at electrolyte/octanol interfaces: A molecular perspective, *J. Phys. Chem. C*, 2020, **124**, 10924–10934.

25 N. Kumar, B. Sadhu and A. E. Clark, Essential Aspects of Solvent Effects and Solution Conditions upon the Modeling and Simulation of Lanthanide and Actinide Complexes, *Rare Earth Elements Actinides: Progress Comput. Sci. Appl.*, 2021, 249–276.

26 J. Sala, E. Guardia and J. Martí, Specific ion effects in aqueous eletrolyte solutions confined within graphene sheets at the nanometric scale, *Phys. Chem. Chem. Phys.*, 2012, **14**, 10799–10808.

27 C. D. Williams, J. Dix, A. Troisi and P. Carbone, Effective polarization in pairwise potentials at the graphene–electrolyte interface, *J. Phys. Chem. Lett.*, 2017, **8**, 703–708.

28 B. J. Kirby and P. Jungwirth, Charge scaling manifesto: A way of reconciling the inherently macroscopic and microscopic natures of molecular simulations, *J. Phys. Chem. Lett.*, 2019, **10**, 7531–7536.

29 K.-Y. Chiang, T. Seki, C.-C. Yu, T. Ohto, J. Hunger and M. Bonn, Nagata The dielectric function profile across the water interface through surface-specific vibrational spectroscopy and simulations, *Proc. Natl. Acad. Sci. U. S. A.*, 2022, **119**, e2204156119.

30 S. S. Lee, A. Koishi, I. C. Bourg and P. Fenter, Ion correlations drive charge overscreening and heterogeneous nucleation at solid–aqueous electrolyte interfaces, *Proc. Natl. Acad. Sci. U. S. A.*, 2021, **118**, e2105154118.

31 A. Uysal, H. Zhou, G. Feng, S. S. Lee, S. Li, P. Fenter, P. T. Cummings, P. F. Fulvio, S. Dai and J. K. McDonough, *et al.*, Structural origins of potential dependent hysteresis at the electrified graphene/ionic liquid interface, *J. Phys. Chem. C*, 2014, **118**, 569–574.

32 D. G. Sangiovanni, R. Faccio, G. K. Gueorguiev and A. Kakanakova-Georgieva, Discovering atomistic pathways for supply of metal atoms from methyl-based precursors to graphene surface, *Phys. Chem. Chem. Phys.*, 2023, **25**, 829–837.

33 G. Sfuncia, G. Nicotra, F. Giannazzo, B. Pécz, G. K. Gueorguiev and A. Kakanakova-Georgieva, 2D graphiticlike gallium nitride and other structural selectivity in confinement at the graphene/SiC interface, *CrystEngComm*, 2023, **25**, 5810–5817.

34 H. Zhou, A. Uysal, D. M. Anjos, Y. Cai, S. H. Overbury, M. Neurock, J. K. McDonough, Y. Gogotsi and P. Fenter, Understanding Defect-Stabilized Noncovalent Functionalization of Graphene, *Adv. Mater. Interfaces*, 2015, **2**, 1500277.

35 S. E. Lee, A. J. Carr, R. R. Kumal and A. Uysal, Monovalent ion–graphene oxide interactions are controlled by carboxylic acid groups: Sum frequency generation spectroscopy studies, *J. Chem. Phys.*, 2024, 160.

36 S. M. Piontek and E. Borguet, Vibrational Spectroscopy of Geochemical Interfaces, *Surf. Sci. Rep.*, 2023, 100606.

37 M. Xu, D. Liu and H. C. Allen, Ethylenediamine at air/liquid and air/silica interfaces: protonation versus hydrogen bonding investigated by sum frequency generation spectroscopy, *Environ. Sci. Technol.*, 2006, **40**, 1566–1572.

38 C. Zhan, M. R. Cerón, S. A. Hawks, M. Otani, B. C. Wood, T. A. Pham, M. Stadermann and P. G. Campbell, Specific ion effects at graphitic interfaces, *Nat. Commun.*, 2019, **10**, 4858.

39 J. A. Greathouse, R. J. O'Brien, G. Bemis and R. T. Pabalan, Molecular dynamics study of aqueous uranyl interactions with quartz (010), *J. Phys. Chem. B*, 2002, **106**, 1646–1655.

40 N. Kumar, Exclusive ion recognition using host–guest sandwich complexes, *Phys. Chem. Chem. Phys.*, 2024, **26**, 3152–3158.

41 N. Zarayeneh, N. Kumar, A. Kalyanaraman and A. E. Clark, Dynamic Community Detection Decouples Multiple Time Scale Behavior of Complex Chemical Systems, *J. Chem. Theory Comput.*, 2022, **18**, 7043–7051.

42 N. Kumar and A. E. Clark, Unexpected inverse correlations and cooperativity in ion-pair phase transfer, *Chem. Sci.*, 2021, **12**, 13930–13939.

43 J. Neuefeind, L. Soderholm and S. Skanthakumar, Experimental coordination environment of uranyl (VI) in aqueous solution, *J. Phys. Chem. A*, 2004, **108**, 2733–2739.

44 D. Hagberg, G. Karlström, B. O. Roos and L. Gagliardi, The coordination of uranyl in water: A combined quantum chemical and molecular simulation study, *J. Am. Chem. Soc.*, 2005, **127**, 14250–14256.

45 O. Suleimenov, T. M. Seward and J. Hovey, A spectrophotometric study on uranyl nitrate complexation to 150C, *J. Solution Chem.*, 2007, **36**, 1093–1102.

46 H. A. Thompson, G. E. Brown and G. A. Parks, XAFS spectroscopic study of uranyl coordination in solids and aqueous solution, *Am. Mineral.*, 1997, **82**, 483–496.

47 L. Rao and G. Tian, Thermodynamic study of the complexation of uranium (VI) with nitrate at variable temperatures, *J. Chem. Thermodyn.*, 2008, **40**, 1001–1006.

48 Y. Zhang, H. B. de Aguiar, J. T. Hynes and D. Laage, Water structure, dynamics, and sum-frequency generation spectra at electrified graphene interfaces, *J. Phys. Chem. Lett.*, 2020, **11**, 624–631.

49 F. Jiménez-Ángeles, K. J. Harmon, T. D. Nguyen, P. Fenter and M. O. de la Cruz, Nonreciprocal interactions induced by water in confinement, *Phys. Rev. Res.*, 2020, **2**, 043244.

50 M. Gordillo and J. Martí, Structure of water adsorbed on a single graphene sheet, *Phys. Rev. B*, 2008, **78**, 075432.

51 T. A. Ho and A. Striolo, Polarizability effects in molecular dynamics simulations of the graphene-water interface, *J. Chem. Phys.*, 2013, **138**, 054117.

52 H. Eslami and N. Heydari, Hydrogen bonding in water nanoconfined between graphene surfaces: a molecular dynamics simulation study, *J. Nanopart. Res.*, 2014, **16**, 1–10.

53 M. Abraham, T. Murtol, R. Schulz, S. Pall, J. Smith, B. Hess and E. Lindhal, GROMACS: High performance molecular simulations through multi-level parallelism from laptops to supercomputers, *SoftwareX*, 2015, **1–2**, 19–25.

54 L. Martínez, R. Andrade, E. G. Birgin and J. M. Martínez, PACKMOL: A package for building initial configurations for molecular dynamics simulations, *J. Comput. Chem.*, 2009, **30**, 2157–2164.

55 I. S. Joung and T. E. Cheatham III, Determination of alkali and halide monovalent ion parameters for use in explicitly solvated biomolecular simulations, *J. Phys. Chem. B*, 2008, **112**, 9020–9041.

56 W. L. Jorgensen, J. Chandrasekhar, J. D. Madura, R. W. Impey and M. L. Klein, Comparison of simple potential functions for simulating liquid water, *J. Chem. Phys.*, 1983, **79**, 926–935.

57 V. Hornak, R. Abel, A. Okur, B. Strockbine, A. Roitberg and C. Simmerling, Comparison of multiple Amber force fields and development of improved protein backbone parameters, *Proteins: Struct., Funct., Bioinf.*, 2006, **65**, 712–725.

58 K. Vanommeslaeghe, E. Hatcher, C. Acharya, S. Kundu, S. Zhong, J. Shim, E. Darian, O. Guvench, P. Lopes and I. Vorobyov, *et al.*, CHARMM general force field: A force field for drug-like molecules compatible with the CHARMM all-atom additive biological force fields, *J. Comput. Chem.*, 2010, **31**, 671–690.

59 P. Guilbaud and G. Wipff, Hydration of uranyl (UO_2^{2+}) cation and its nitrate ion and 18-crown-6 adducts studied by molecular dynamics simulations, *J. Phys. Chem.*, 1993, **97**, 5685–5692.

60 M. Baaden, M. Burgard and G. Wipff, TBP at the wateroil interface: the effect of TBP concentration and water acidity investigated by molecular dynamics simulations, *J. Phys. Chem. B*, 2001, **105**, 11131–11141.